Multiphonon interaction and thermal conductivity in half-Heusler LuNiBi

Yongheng Li,[1] Jie Chen,[2] Cong Lu,[3,*] Hiroshi Fukui,[4] Xiaoxia Yu,[5] Chunyang Li,[6] Jing Zhao,[6] Xueyun Wang,[1] Wenhong Wang,[2,†] and Jiawang Hong[1,‡]

[1]*School of Aerospace Engineering, Beijing Institute of Technology, Beijing 100081, China*
[2]*School of Electronic and Information Engineering, Tiangong University, Tianjin 300387, China*
[3]*Multi-disciplinary Research Division, Institute of High Energy Physics, Chinese Academy of Sciences, Beijing 100049, China*
[4]*Precision Spectroscopy Division, Japan Synchrotron Radiation Research Institute (SPring-8), 1-1-1 Kouto, Sayo, Hyogo 679-5198, Japan*
[5]*School of Mechanical Engineering, Yanshan University, Qinhuangdao 066004, China*
[6]*School of Mechatronical Engineering, Beijing Advanced Innovation Center for Intelligent Robots and Systems, Beijing Institute of Technology, Beijing 100081, China*

(Received 3 October 2023; revised 22 February 2024; accepted 28 March 2024; published 1 May 2024)

Half-Heusler compounds are promising candidates for thermoelectrics. The exploration of multiphonon interaction, including four-phonon interaction, in half-Heusler compounds contributes to the deep understanding of thermal transport, which is helpful to optimize thermoelectric properties. In this work, LuNiBi is taken as the typical half-Heusler compound to investigate multiphonon interaction and thermal conductivity. By employing inelastic x-ray scattering and first-principles calculations, we confirm that the low thermal conductivity κ of LuNiBi is closely related to its small group velocity compared with many other half-Heusler compounds. The noteworthy four-phonon scattering between parallel flat acoustic phonon bands is validated through a combination of experiment and calculation, which may be related to its rattlinglike characteristic. Additionally, the calculation confirms the four-phonon scattering further effectively decreases the thermal conductivity at high temperature. The significant four-phonon scattering processes are associated with weakened three-phonon scattering processes due to critical selection rules; this occurs both around parallel flat acoustic phonon bands and in the 13–15 meV energy region. Our work highlights the significance of multiphonon scattering processes, including four-phonon interaction, which plays an important role in the thermal properties of half-Heusler materials.

DOI: 10.1103/PhysRevB.109.174302

I. INTRODUCTION

Half-Heusler compounds have gained significant attention as promising thermoelectric materials [1–4]. The efficiency of thermoelectric materials depends on the dimensionless figure of merit $zT = S^2\sigma/(\kappa_l + \kappa_e)T$, where S is the Seebeck coefficient, σ is the electrical conductivity, κ_l is the lattice thermal conductivity, κ_e is electronic thermal conductivity, and T is the temperature. The half-Heusler compounds usually possess good electronic property such as in ZrCoSb, ZrNiSn, etc., contributing to the large thermoelectric power factor $S^2\sigma$ [5–7]. However, the high thermal conductivity of half-Heusler compounds often limits their thermoelectric conversion efficiency [8,9]. Various approaches relying on external means to regulate thermal conductivity have been extensively studied. Many strategies for reducing the thermal conductivity of half-Heusler compounds have been proposed such as doping engineering, grain boundary engineering, etc. [10–12]. Besides, many researchers are actively searching for half-Heusler materials with intrinsic low lattice thermal conductivity [13–15]. Understanding the intrinsic phonon-phonon interaction in half-Heusler compounds is favorable to optimize the thermoelectric conversion efficiency. Although theories like the Boltzmann transport equation have been widely used to elucidate the micromechanisms of lattice thermal transport properties in half-Heusler materials, such as PCdNa, BaBiK, etc. [13,16–19], there are few experiments to reveal the intrinsic phonon-phonon interaction which relies on the inelastic scattering techniques.

The *REYZ* type half-Heusler compounds (*RE* is a rare-earth element, *Y* is a transition element, *Z* is a heavy main group element) attract attention due to their rich and intriguing physical phenomena and favorable properties, such as large magnetoresistance and high carrier mobility in LuPtBi and YPtBi [20,21], weak antilocalization effect and noncentrosymmetry superconductivity in LuPdBi [22], topological insulators LaPtBi [23], etc. Recently, LuNiBi has emerged as a material exhibiting weak antilocalization effect, large magnetoresistance, and even a topological phase [24–26]. Its thermoelectric properties have also been investigated theoretically, including electronic and thermal transport [27,28]. In spite of this, there is still a lack of comprehensive understanding of the intrinsic phonon-phonon interaction in LuNiBi. On the one hand, there are few inelastic scattering experiments on LuNiBi. On the other hand, though four-phonon scattering

*lucong@ihep.ac.cn
†wenhong.wang@iphy.ac.cn
‡hongjw@bit.edu.cn

has become a popular theory to further comprehend thermal transport property [29,30], there are few studies that apply high-order phonon-phonon interactions to half-Heusler materials. The four-phonon scattering processes can affect not only the phonon shift such as in $Cs_2AgBiBr_6$ [31] but also the phonon linewidth such as in $AgCrSe_2$. The four-phonon scattering usually leads to the phonon lifetime $\tau_4^{-1} \sim \omega^4 T^2$. It indicates the four-phonon scattering processes are more sensitive to the temperature than three-phonon scattering processes, which usually lead to $\tau_3^{-1} \sim \omega^2 T$. Thus the four-phonon scattering processes can further affect the thermal conductivity at high temperature.

Here, we explore the multiphonon interaction, both three- and four-phonon scattering, of LuNiBi by inelastic x-ray scattering (IXS) experiment and first-principles calculation. Among various half-Heusler materials, the low thermal conductivity of LuNiBi is closely related to its low group velocity. Interestingly, we observe parallel flat phonon bands around ~ 8 meV near the zone boundary and the *W*-*V* direction of LuNiBi, which can be attributed to the rattlinglike characteristic in its structure. The obvious four-phonon scattering is revealed between parallel flat acoustic phonon bands, which is confirmed by both experiment and calculation. Moreover, the four-phonon scattering between 13 and 15 meV also has an obvious effect on thermal conductivity due to the weak three-phonon scattering in that energy region, which results from the limitations of critical three-phonon selection rules. This work sheds light on the potential significance of high-order phonon interaction in other half-Heusler materials with more anharmonicity.

II. EXPERIMENTS AND CALCULATIONS

The high quality LuNiBi single crystal was prepared by a Bi flux method, as described in previous work [32]. The BL35XU beamline in SPring-8 [33] was utilized for inelastic x-ray scattering measurement with 21.7 keV incident energy at 300 K. The measurements were performed with a resolution of 1.5 meV and a momentum resolution of 0.05, in units of reciprocal lattice ($2\pi/a$). The [111] surface of the LuNiBi single crystal was good quality, approximately 1×1 mm in size, and was oriented perpendicular to the x-ray beam. Due to the large thickness of the samples (~ 0.8 mm), the reflection mode was employed in this experiment. The vacuum environment was maintained throughout the entire experiment in order to protect the samples. The appropriate Brillion zone Q= [2,2,2] for measuring the phonon dispersion was selected using our in-house code. The damped harmonic oscillator (DHO) model convoluted with the resolution function was employed to obtain a reasonable phonon energy and phonon linewidth; it is described as

$$I(E) = R\left[A\frac{\left\{\frac{1}{2} \pm \frac{1}{2} + n(|E|)\right\} \times E\Gamma_{\mathrm{LW}}}{\left(E^2 - {E_c}^2\right)^2 + (\Gamma_{\mathrm{LW}}x)^2} + B\right], \quad (1)$$

where R is the resolution function, E_c is the renormalized phonon energy, $n(E)$ is the Bose-Einstein distribution function at phonon energy transfer E, Γ_{LW} is the phonon full width at half maximum, A is amplitude, and B is a constant.

The temperature-dependent phonon dispersion was calculated based on the temperature-dependent effective potential (TDEP) method [34,35]. The *ab initio* molecular dynamics (AIMD) was conducted with the Vienna *ab initio* simulation package (VASP) [36]. The generalized gradient approximation (GGA) [37] and 420 eV kinetic energy cutoff were chosen in the calculations. The electronic energy tolerance was set as 10^{-5}. The simulations were run with a total number of 10 ps with 1 fs/step for 300 and 700 K. The cubic-like superlattice with 126 atoms was spanned by the vectors $[-1/2, 1/2, 2]a$, $[-3/2, 3/2, -1]a$, $[-3/2, -3/2, 0]a$, where $a = 6.41$ Å is the fcc lattice constant. The AIMD was conducted with the canonical ensemble using a Nosé-Hoover thermostat. Such cubiclike supercells can significantly lower the computational cost associated with obtaining converged phonon dispersions [38,39]. The converged cutoff radii of the second-order force constant, third-order force constant, and fourth-order force constant are set as 6.5, 6.5, and 5.5 Å, respectively. The thermal conductivity was calculated with FOURPHONON, which includes the thermal conductivity with four-phonon scattering [40,41]. Due to the large amount of computation for four-phonon scattering, the converged q mesh was set as $8 \times 8 \times 8$. The convergence tests of cutoff radii and q mesh are shown in Figs. S1 and S2 (see Supplemental Material [42]), respectively. The phonon self-energy $\Sigma_{\vec{q},j}$ was also calculated, which can be described as

$$\begin{aligned}\Sigma_{\vec{q},j} &\approx \Sigma^{(1)}_{\vec{q},j}(\Omega) + \Sigma^{(2)}_{\vec{q},j}(\Omega) \\ &= \left[\Delta^{(1)}_{\vec{q},j}(\Omega) + i\Gamma^{(1)}_{\vec{q},j}(\Omega)\right] + \left[\Delta^{(2)}_{\vec{q},j}(\Omega) + i\Gamma^{(2)}_{\vec{q},j}(\Omega)\right]. \quad (2)\end{aligned}$$

The imaginary part $\Gamma^{(1)}_{\vec{q},j}(\Omega)$ is associated with three-phonon interaction and isotopic scattering [43] while the $\Gamma^{(2)}_{\vec{q},j}(\Omega)$ is related to four-phonon interaction [44–46]. The detailed formula of the phonon self-energy calculation is shown in the phonon self-energy section in the Supplemental Material [42].

III. RESULTS AND DISCUSSION

The LuNiBi exhibits a typical half-Heusler structure, belonging to the *F*-43*m* space group. The structure comprises three interpenetrating face-centered cubic (fcc) sublattices along with one unoccupied fcc sublattice. The relaxed lattice constants $a = 6.41$ Å, which is reasonably 1.1% larger than the experimental lattice constants $a = 6.34$ Å [32]. As shown in Fig. 1(a), the nearest Lu-Bi bond is $a/2$ while the nearest Lu-Ni and Ni-Bi bonds are $a\sqrt{3}/4$. These two different shortest bond lengths provide the possibility of a rattlinglike phenomenon [18].

As shown in Fig. 1(b), the calculated phonon dispersion at 300 K agrees well with the inelastic x-ray experiment results. Notably, the region between 7.5 and 10 meV displays flat phonon bands when the transverse acoustic (TA) phonons approach the zone boundary, particularly near the *W* and *V* points, as illustrated in the pink shaded area in Fig. 1(b). Between *W* and *V*, there are two nearly parallel transverse acoustic phonon bands. This region corresponds to the first peak of the vibrational density of states (VDOS) as illustrated in Fig. 1(c). Between 13 and 15 meV, the optical phonon bands contribute to the second peak of VDOS as shown in the green shaded area in Fig. 1(b). It is worth noting that most of these optical phonons in this energy region still have large

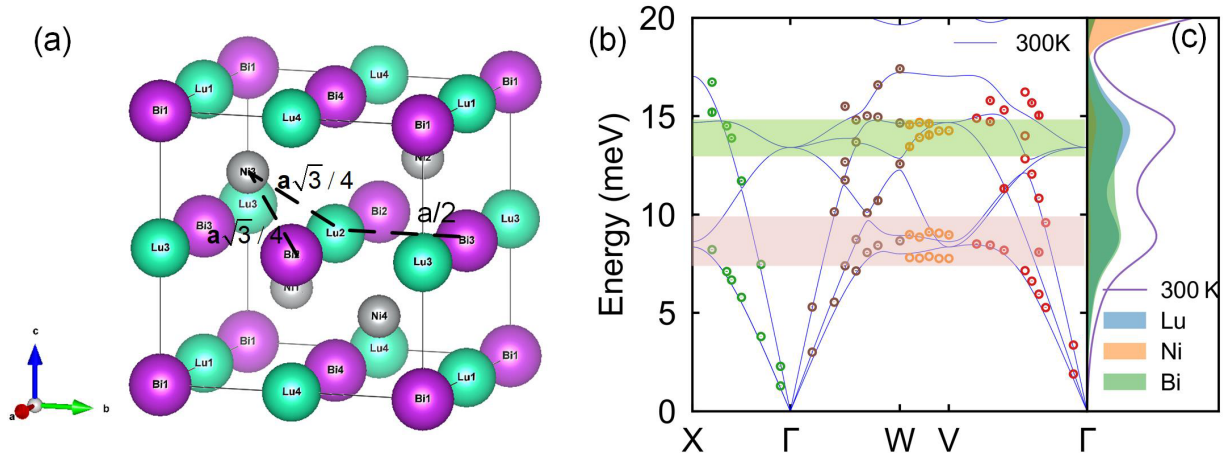

FIG. 1. (a) The structure of LuNiBi. The picture is shown with VESTA [47]. (b) The phonon dispersion of LuNiBi at 300 K. The dots are results from IXS experiment. The lines are calculated with force constants at 300 K. The symbols X, Γ, W, and V represent (0, 1, 0), (0, 0, 0), (0.5, 1, 0), and (1, 1, 0) in the conventional basis, respectively. (c) The vibrational density of states for LuNiBi at 300 K.

slopes, indicating the large group velocity. Below 15 meV, the vibrations are primarily dominated by the heavy element Lu and Bi, as depicted in Fig. 1(c).

Based on the VDOS, we have calculated the average phonon energy of various atoms with $\overline{\omega_i} = \frac{\int d\omega_i g(\omega_i)\omega_i}{\int d\omega_i g(\omega_i)}$, where ω_i is the phonon energy of the ith kind of atoms and $g(\omega_i)$ is the VDOS of the ith kind of atom. The $\overline{\omega}_{\mathrm{Lu}}$, $\overline{\omega}_{\mathrm{Ni}}$, and $\overline{\omega}_{\mathrm{Bi}}$ are 12.36, 19.38, and 11.97 meV, respectively. The total average phonon frequency $\overline{\omega}_{\mathrm{average}}$ is 14.57 meV. Notably, the $\overline{\omega}_{\mathrm{Lu}}$ and $\overline{\omega}_{\mathrm{Bi}}$ with heavy elements are much smaller than the $\overline{\omega}_{\mathrm{average}}$ while the $\overline{\omega}_{\mathrm{Ni}}$ with light Ni atoms is much larger than the $\overline{\omega}_{\mathrm{average}}$. The $\overline{\omega}_{\mathrm{min}}/\overline{\omega}_{\mathrm{max}} = \overline{\omega}_{\mathrm{Bi}}/\overline{\omega}_{\mathrm{Ni}} = 0.617$. The distribution of average phonon energy of various atoms in LuNiBi is very similar to that of some half-Heusler compounds like BiBaK, RhLaTe, etc., which are known to possess low thermal conductivity and are referred to as structures with rattler characteristics [18]. Therefore, LuNiBi could also be referred to as a structure with rattlinglike characteristics, which results in the flat phonon bands between 7.5 and 10 meV.

The group velocity and elastic constants were extracted from the IXS experiment as shown in Table I. The calculated group velocity and elastic constants are slightly lower than the IXS results, which may be related to the overestimation of lattice constants due to the GGA potential. In general, the experiment agrees well with the calculation. The C_{11} of LuNiBi is only about half of that for ZrCoSb and ZrCoBi, which indicates the lattice of LuNiBi is much softer than ZrCoSb, etc. [48]. Consequently, LuNiBi is expected to possess the low average group velocity due to the presence of heavy elements Lu and Bi, as shown in Fig. 2(a). This characteristic will contribute to its low thermal conductivity compared to other half-Heusler materials. However, as shown in the shaded region of Fig. 2(b), the optical phonon bands around 14 meV still possess large group velocity, which may still contribute to the total thermal conductivity.

Interestingly, we observed the intriguing multiphonon interaction, particularly four-phonon interaction, in LuNiBi. Notably, there are parallel TAs around the zone boundary W and V, as well as the whole W-V direction. As described with red and blue lines in Fig. 3(a), two nearly parallel phonon peaks are shown with the q vector increasing from 0.1 to 0.5 along the W-V direction. Such parallel flat acoustic phonon bands usually limit the three-phonon scattering while they can lead to strong four-phonon scattering, such as in $AgCrSe_2$ [44]. Figure 3(b) shows a comparison of the phonon linewidth of TA1 along the X-Γ-W-V-Γ direction at 300 K between the calculation and the experiment. It also demonstrates that the calculation including both three- and four-phonon scattering agrees much better with experimental results than that only including three-phonon scattering, especially around parallel phonon bands along the W-V direction.

To clearly show the effect of four-phonon interaction, we calculated the phonon line shape and then extracted the imaginary part, which is related to the phonon linewidth. As marked with ellipse in Figs. 3(c) and 3(d), around the eigenfrequency of TA1 7.7 meV, there is no peak from three-phonon scattering in the imaginary part of the phonon self-energy, while an obvious peak from four-phonon scattering is present. Particularly, when temperature increases from 300 to 700 K, the intensity of the four-phonon scattering related peak significantly increases. However, there is little change in the imaginary part of the phonon self-energy related to three-phonon scattering around the eigenfrequency of TA1 7.7 meV.

TABLE I. The group velocity and elastic constants of LuNiBi from inelastic x-ray scattering experiment and calculation at 300 K. The mass density is 11.21×10^3 kg/m^3. The units of group velocity and elastic constants are m/s and GPa, respectively.

	$v_{GX_{\mathrm{TA1}}}$	$v_{GW_{\mathrm{TA1}}}$	$v_{GV_{\mathrm{TA1}}}$	$v_{GX_{\mathrm{LA}}}$	$v_{GW_{\mathrm{LA}}}$	$v_{GV_{\mathrm{LA}}}$	C_{11}	C_{44}	C_{12}
IXS	2000	2091	2080	3859	3680	3695	166.94	44.84	67.56
Calc	1814	1813	1803	3796	3553	3614	161.53	36.89	57.52

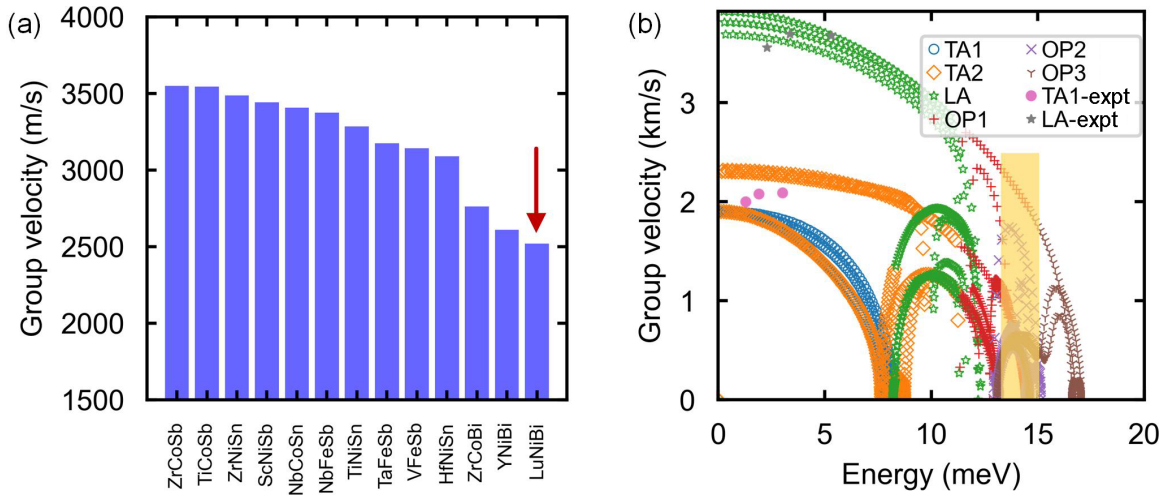

FIG. 2. (a) The comparison of group velocity between LuNiBi and other typical half-Heusler materials [14]. (b) The energy-dependent group velocity of LuNiBi. The solid dots are extracted from IXS experiment. Others are based on calculation.

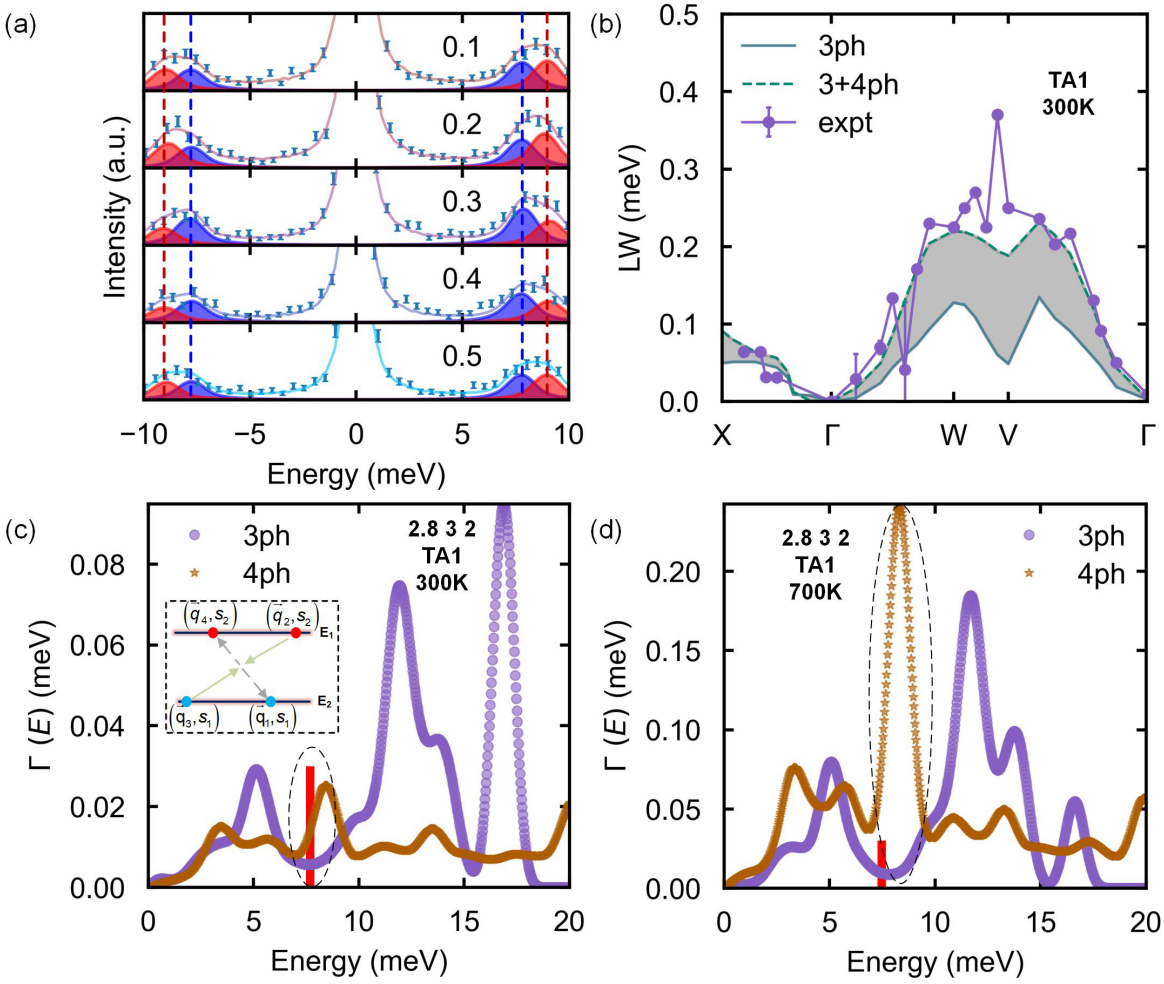

FIG. 3. (a) The inelastic x-ray scattering spectra of the TA phonons in LuNiBi along the *W*-*V* direction at 300 K. The blue and red peaks indicate two parallel transverse acoustic phonons, which are marked with blue and red parallel lines. The numbers 0.1–0.5 indicate the different q positions, which correspond to $[2.5 + q,\ 3,\ 2]$. (b) The phonon linewidth Γ_{LW} of TA1 along *X*-Γ-*W*-*V*-Γ at 300 K. The imaginary part of the phonon self-energy $\Gamma(E)$ of TA1 at 300 K (c) and at 700 K (d) at [2.8, 3, 2]. The inset picture in (c) describes the phonon interaction between parallel phonon bands. The dots and stars indicate the contribution from three-phonon interaction and four-phonon interaction, respectively. The red bar in the ellipse indicates the eigenfrequency of TA1.

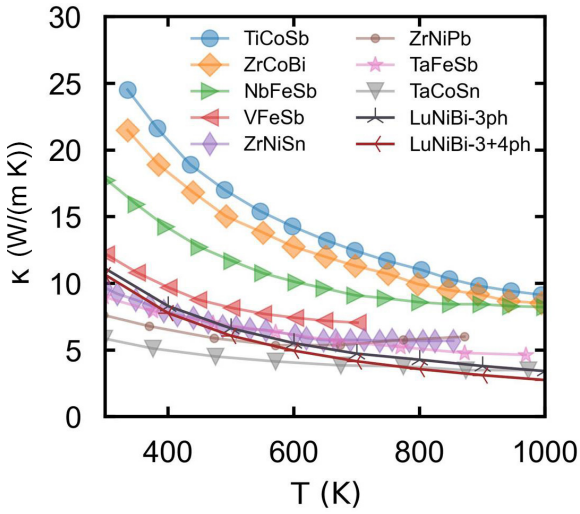

FIG. 4. The comparison of thermal conductivity between LuNiBi and other half-Heusler materials [3,14,51–55].

This suggests that, in determining the line shape of TA1 at [2.8, 3, 2], the impact of four-phonon scattering processes is more significant than that of three-phonon scattering processes. This is attributed to the greater significance of the peaks around the eigenfrequency in phonon self-energy [49]. The strong four-phonon scattering can be understood with the inset picture in Fig. 3(c). The energy conservation can be automatically satisfied with $\omega_{q_2,s_2} + \omega_{q_3,s_1} = \omega_{q_1,s_1} + \omega_{q_4,s_2}$ between the parallel phonon bands. The conservation of momentum follows the parallelogram rule $\vec{q_2} + \vec{q_3} = \vec{q_1} + \vec{q_4} + \vec{G}$, where $\vec{G}$ is the reciprocal lattice vector. The presence of parallel TAs makes it easier to satisfy the conservation of energy and momentum required for four-phonon scattering simultaneously [49]. When the temperature increases, the more phonons are excited and participate in the process of four-phonon scattering. However, three-phonon scattering is limited with critical selection rules. In parallel acoustic phonon bands, only specific reciprocal points can be satisfied [49]. The rattlinglike characteristic in LuNiBi should be closely related to such formation of parallel flat phonon bands, leading to non-negligible four-phonon scattering, especially at high temperature. This suggests that in more anharmonic half-Heusler materials with more obvious rattler behavior, such as PCdNa, BaBiK, etc. [18], there may be much stronger four-phonon scattering between parallel flat phonon bands. This effect could even resemble the resonant four-phonon scattering observed in $AgCrSe_2$ and AgI [49,50].

As shown in Fig. 4, the thermal conductivity of LuNiBi ($\sim$ 10.64 W/mK) is significantly smaller than that of ZrCoBi at 300 K [51], in agreement with its relatively small elastic constants and group velocity as previously predicted. It is also lower than some other typical thermoelectric half-Heusler materials such as TiCoSb [52], NbFeSb [4], etc. Further comparisons of thermal conductivity between LuNiBi and other half-Heusler materials in Table S1 and Fig. S3 [42] reveal that LuNiBi can be considered as a half-Heusler material with low thermal conductivity. Some half-Heusler materials such as TaCoSn [53] and ZrNiPb [54] possess lower thermal conductivity than that of LuNiBi at 300 K. As the temperature increases up to 1000 K, the thermal conductivity of LuNiBi decreases by approximately half, making it comparable to TaCoSn [48]. Moreover, the four-phonon scattering further decreases the thermal conductivity of LuNiBi, particularly when temperature increases. With the inclusion of four-phonon scattering, the temperature-dependent thermal conductivity of LuNiBi changes from $\kappa \sim T^{-1}$ to $\kappa \sim T^{-1.11}$. The contribution of four-phonon scattering should be closely related to the parallel flat phonon bands mentioned earlier.

Subsequently, we further explore the thermal transport and multiphonon interaction in LuNiBi. The cumulative thermal conductivity κ_{zz} of LuNiBi along the z direction at 700 K is shown in Fig. 5(a). The phonons below 15 meV contribute the most to the thermal conductivity, with the acoustic phonon bands contributing 85.34% and the optical phonon bands contributing 14.66% to the total thermal conductivity. It is similar to the cumulative thermal conductivity of LuNiBi at 300 K as shown in Fig. S4(a), 82.70% from acoustic phonons and 17.30% from optical modes. The contribution from optical phonon bands is closely related to the large group velocity as mentioned before. Energy larger than 15 meV contributes little to the total lattice thermal conductivity and thus we do not discuss these modes here. Totally, the three-phonon interaction dominates the contribution to the thermal conductivity of LuNiBi. However, there are two energy regions, 7.5–10 meV and 13–15 meV, that show an obvious contribution from the four-phonon interaction as shown in Fig. 5(b) and Fig. S4b [42]. When temperature increases to 700 K, the two energy regions exhibit a more obvious contribution from four-phonon interaction than those at 300 K as marked with ellipses in Fig. 5(b). The first region, ranging from 7.5 to 10 meV, corresponds to the location of parallel flat TA phonons, where the first prominent peak of VDOS is observed as shown in Fig. 1(c). Their impact on thermal conductivity is even more significant than that of the optical region, as depicted with red bars in Fig. 5(b). It indicates the much stronger four-phonon scattering between parallel flat phonon bands than other locations of phonon bands. The second region, ranging from 13 to 15 meV, corresponds to the second prominent peak of VDOS as shown in Fig. 1(c). Now we explore the reason for such obvious four-phonon interaction in the two energy regions.

The energy-dependent phonon linewidth at 700 K in Fig. 5(c) further illustrates the anharmonic phonon scattering process in detail. The region between 7.5 and 10 meV exhibits the peaklike shape in the four-phonon scattering related linewidth as shown in the olive ellipse in Fig. 5(c), which corresponds to the peaklike shape of the four-phonon scattering phase space as marked with the olive ellipse in Fig. 5(d). Between 5 and 7.5 meV, the phonon linewidth resulting from three-phonon scattering is much larger than that from four-phonon scattering, agreeing with three-phonon scattering predominantly affecting the total thermal conductivity. However, the three-phonon scattering phase space between 7.5 and 10 meV notably decreases as shown in the olive ellipse in Fig. 5(d). It further supports the notion that the presence of parallel phonon bands limits the three-phonon interaction while favoring four-phonon scattering.

Moving on to the second region with obvious four-phonon interaction, ranging from 13 to 15 meV, a peaklike shape

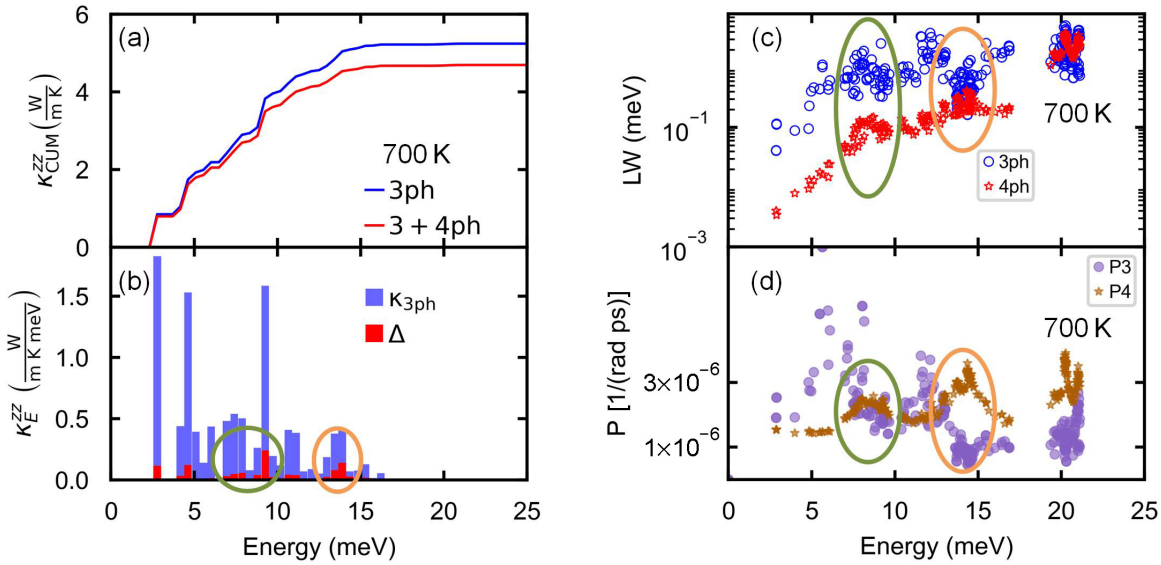

FIG. 5. (a) The cumulative thermal conductivity of LuNiBi at 700 K. The blue and red lines in the graph indicate the thermal conductivity when considering only three-phonon interaction and when considering both three- and four-phonon interactions, respectively. (b) The energy-dependent thermal conductivity of LuNiBi at 700 K. The blue bars indicate the energy-dependent thermal conductivity from three-phonon interaction κ_{3ph}. The red bars indicate the contribution from four-phonon interaction, which is described as $\Delta = |\kappa_{3+4ph} - \kappa_{3ph}|$. (c) The energy-dependent phonon linewidth of LuNiBi at 700 K. The circles and stars indicate the energy-dependent phonon linewidth from three-phonon interaction and four-phonon interaction, respectively. (d) The energy-dependent phase space of LuNiBi at 700 K. The circles and stars indicate the phase space for three-phonon interaction and four-phonon interaction, respectively. The regions marked with olive and orange ellipses indicate where the four-phonon interaction is obvious.

of the linewidth from four-phonon scattering is observed in Fig. 5(c), along with a peaklike shape in the four-phonon scattering phase space in Fig. 5(d). However, the three-phonon scattering becomes weaker in this region than in the other energy region, resulting in a valley of the linewidth and phase space for three-phonon scattering between 13 and 15 meV, as shown in the orange ellipse of Fig. 5(c) and 5(d). The decreased three-phonon scattering in this region is mainly related to the decrease of AOO as shown in the region marked with an orange ellipse in Fig. S5 [42] (A is acoustic phonon and O is optical phonon). Such decrease is related to the classical AOO selection rules 1 and 2. AOO selection rule 1 is that AOO processes cannot occur when the frequencies of acoustic phonons exceed the optical phonon bandwidth $\Delta\omega_o$ [56]. LuNiBi possesses the optical bandwidth $\Delta\omega_o \sim 10$ meV, as illustrated by the phonon bands with sorted polarization in Fig. S5(b) [42,57–60]. As shown in Fig. 1(b) and Fig. S5(b) [42], the acoustic phonon can really approach and even go beyond the $\Delta\omega_o$, based on the IXS and calculation, and then in this region the AOO starts to decrease [61]. AOO selection rule 2 is that if the group velocities of the optical phonons are lower than those of the acoustic phonons, the AOO process is prohibited when both optical phonons originate from the same phonon branch [61]. As shown in the shaded region in Fig. 2(b), when optical modes approach 15 meV, the group velocity of most optical modes decreases sharply. Thus, the decrease of AOO should be associated with the critical AOO selection rule 2 [61]. However, the four-phonon scattering processes are easier to achieve compared to three-phonon scattering due to being less restrictive [62]. Thus the four-phonon interaction becomes obvious between 13 and 15 meV. In all, in these two regions marked with ellipses in Figs. 5(b)–5(d), the strong limitations imposed by the three-phonon scattering selection rules make the effect of four-phonon scattering on thermal conductivity more obvious.

IV. CONCLUSION

The low thermal conductivity of half-Heusler material LuNiBi is primarily due to its low group velocity, which is closely related to the presence of heavy elements Lu and Bi in the material system. Nevertheless, the parallel flat TA phonon bands related to rattlinglike characteristics contribute to the obvious four-phonon scattering, which is confirmed by IXS experiment and calculation. The parallel phonon bands satisfy energy and momentum conservation more effectively for four-phonon scattering than for three-phonon scattering. In addition, the energy region between 13 and 15 meV shows clear evidence of four-phonon scattering, which is intensified by the weak three-phonon scattering due to the limitation imposed by critical selection rules. This work unveils the relation between four-phonon scattering and rattlinglike characteristics. It emphasizes the importance of considering four-phonon scattering in half-Heusler materials with exceptionally strong anharmonicity, such as BiBaK, PCdNa, and others.

ACKNOWLEDGMENTS

This work at Beijing Institute of Technology was supported by the National Key Research and Development Program of China (Grant No. 2021YFA1400300), the National Natural Science Foundation of China (Grant No. 12172047), and Beijing National Laboratory for Condensed Matter Physics

(2023BNLCMPKF003) and Graduate Technological Innovation Project of Beijing Institute of Technology (Grant No. 2023YCXZ002). A portion of this work was supported by the National Natural Science Foundation of China (Grant No. 12274321). Theoretical calculations were performed using resources of the Supercomputer Centre in Chongqing. The synchrotron radiation experiments were performed at BL35XU of SPring-8 with the approval of the Japan Synchrotron Radiation Research Institute (JASRI) (Proposal No. 2021B1551).

[1] T. Zhu, C. Fu, H. Xie, Y. Liu, and X. Zhao, High efficiency half-Heusler thermoelectric materials for energy harvesting, Adv. Energy Mater. **5**, 1500588 (2015).

[2] J.-W. G. Bos and R. A. Downie, Half-Heusler thermoelectrics: A complex class of materials, J. Phys.: Condens. Matter **26**, 433201 (2014).

[3] C. Fu, S. Bai, Y. Liu, Y. Tang, L. Chen, X. Zhao, and T. Zhu, Realizing high figure of merit in heavy-band *p*-type half-Heusler thermoelectric materials, Nat. Commun. **6**, 8144 (2015).

[4] C. Fu, T. Zhu, Y. Liu, H. Xie, and X. Zhao, Band engineering of high performance *p*-type FeNbSb based half-Heusler thermoelectric materials for figure of merit $zT > 1$, Energy Environ. Sci. **8**, 216 (2015).

[5] Q. Zhang, P. Xie, C. Liu, S. Li, X. Lei, L. Huang, G. Yuan, and F. Cai, Enhanced thermoelectric performance of hafnium free *n*-type ZrNiSn half-Heusler alloys by isoelectronic Si substitution, Mater. Today Phys. **24**, 100648 (2022).

[6] J. Yang, H. Li, T. Wu, W. Zhang, L. Chen, and J. Yang, Evaluation of half-heusler compounds as thermoelectric materials based on the calculated electrical transport properties, Adv. Funct. Mater. **18**, 2880 (2008).

[7] N. Ibrahim, R. A. Ahmed, H. Adri, and I. Reisya, Electronic structures and thermoelectric properties of heavily doped *n*-type ZrCoBi from first principles calculations, Mater. Today Commun. **32**, 103908 (2022).

[8] F. Casper, T. Graf, S. Chadov, B. Balke, and C. Felser, Half-Heusler compounds: Novel materials for energy and spintronic applications, Semicond. Sci. Technol. **27**, 063001 (2012).

[9] W. Xie, A. Weidenkaff, X. Tang, Q. Zhang, J. Poon, and T. M. Tritt, Recent advances in nanostructured thermoelectric half-Heusler compounds, Nanomaterials **2**, 379 (2012).

[10] S. Sakurada and N. Shutoh, Effect of Ti substitution on the thermoelectric properties of (Zr,Hf)NiSn half-Heusler compounds, Appl. Phys. Lett. **86**, 082105 (2005).

[11] S. Liu, Y. Hu, S. Dai, Z. Dong, G. Wu, J. Yang, and J. Luo, Synergistically optimizing electrical and thermal transport properties of ZrCoSb through Ru doping, ACS Appl. Energy Mater. **4**, 13997 (2021).

[12] R. Tranås, O. M. Løvvik, and K. Berland, Attaining low lattice thermal conductivity in half-Heusler sublattice solid solutions: Which substitution site is most effective? Electron. Mater. **3**, 1 (2022).

[13] J. Carrete, W. Li, N. Mingo, S. Wang, and S. Curtarolo, Finding unprecedentedly low-thermal-conductivity half-Heusler semiconductors via high-throughput materials modeling, Phys. Rev. X **4**, 011019 (2014).

[14] W. Ren, X. Shi, Z. Wang, and Z. Ren, Crystallographic design for half-Heuslers with low lattice thermal conductivity, Mater. Today Phys. **25**, 100704 (2022).

[15] H. Miyazaki, T. Tamura, M. Mikami, K. Watanabe, N. Ide, O. M. Ozkendir, and Y. Nishino, Machine learning based prediction of lattice thermal conductivity for half-Heusler compounds using atomic information, Sci. Rep. **11**, 13410 (2021).

[16] J. Shiomi, K. Esfarjani, and G. Chen, Thermal conductivity of half-Heusler compounds from first-principles calculations, Phys. Rev. B **84**, 104302 (2011).

[17] X. Ye, Z. Feng, Y. Zhang, G. Zhao, and D. J. Singh, Low thermal conductivity and high thermoelectric performance via Cd underbonding in half-Heusler PCdNa, Phys. Rev. B **105**, 104309 (2022).

[18] Z. Feng, Y. Fu, Y. Zhang, and D. J. Singh, Characterization of rattling in relation to thermal conductivity: Ordered half-Heusler semiconductors, Phys. Rev. B **101**, 064301 (2020).

[19] S. H. Han, Z. Z. Zhou, C. Y. Sheng, J. H. Liu, L. Wang, H. M. Yuan, and H. J. Liu, High thermoelectric performance of half-Heusler compound BiBaK with intrinsically low lattice thermal conductivity, J. Phys.: Condens. Matter **32**, 425704 (2020).

[20] Z. Hou *et al.*, High electron mobility and large magnetoresistance in the half-Heusler semimetal LuPtBi, Phys. Rev. B **92**, 235134 (2015).

[21] W. Wang, Y. Du, G. Xu, X. Zhang, E. Liu, Z. Liu, Y. Shi, J. Chen, G. Wu, and X. Zhang, Large linear magnetoresistance and Shubnikov-de Hass oscillations in single crystals of YPdBi Heusler topological insulators, Sci. Rep. **3**, 2181 (2013).

[22] G. Xu, W. Wang, X. Zhang, Y. Du, E. Liu, S. Wang, G. Wu, Z. Liu, and X. X. Zhang, Weak antilocalization effect and noncentrosymmetric superconductivity in a topologically nontrivial semimetal LuPdBi, Sci. Rep. **4**, 5709 (2014).

[23] X. M. Zhang, W. H. Wang, E. K. Liu, G. D. Liu, Z. Y. Liu, and G. H. Wu, Influence of tetragonal distortion on the topological electronic structure of the half-Heusler compound LaPtBi from first principles, Appl. Phys. Lett. **99**, 071901 (2011).

[24] W. Al-Sawai, H. Lin, R. S. Markiewicz, L. A. Wray, Y. Xia, S.-Y. Xu, M. Z. Hasan, and A. Bansil, Topological electronic structure in half-Heusler topological insulators, Phys. Rev. B **82**, 125208 (2010).

[25] H. Lin, L. A. Wray, Y. Xia, S. Xu, S. Jia, R. J. Cava, A. Bansil, and M. Z. Hasan, Half-Heusler ternary compounds as new multifunctional experimental platforms for topological quantum phenomena, Nat. Mater. **9**, 546 (2010).

[26] M. Narimani and Z. Nourbakhsh, Topological phase and optical properties of LuNiBi Bulk and nano-layer, Thin Solid. Films **634**, 112 (2017).

[27] M. J. Winiarski and K. Bilińska, Power factors of *p*-type half-Heusler alloys ScNiBi, YNiBi, and LuNiBi by *ab initio* calculations, Acta Phys. Pol. A **138**, 533 (2020).

[28] X. Yu and J. Hong, Absence of phonon gap driven ultralow lattice thermal conductivity in half-Heusler LuNiBi, J. Mater. Chem. C **9**, 12420 (2021).

[29] T. Feng, L. Lindsay, and X. Ruan, Four-phonon scattering significantly reduces intrinsic thermal conductivity of solids, Phys. Rev. B **96**, 161201(R) (2017).

[30] T. Feng and X. Ruan, Quantum mechanical prediction of four-phonon scattering rates and reduced thermal conductivity of solids, Phys. Rev. B **93**, 045202 (2016).

[31] J. Zheng, C. Lin, C. Lin, G. Hautier, R. Guo, and B. Huang, Unravelling ultralow thermal conductivity in perovskite $Cs_2AgBiBr_6$: dominant wave-like phonon tunnelling and strong anharmonicity, npj Comput. Mater. **10**, 30 (2024).

[32] J. Chen, H. Li, B. Ding, Z. Hou, E. Liu, X. Xi, H. Zhang, G. Wu, and W. Wang, Structural and magnetotransport properties of topological trivial LuNiBi single crystals, J. Alloys Compd. **784**, 822 (2019).

[33] A. Q. R. Baron, Y. Tanaka, S. Goto, K. Takeshita, T. Matsushita, and T. Ishikawa, An x-ray scattering beamline for studying dynamics, J. Phys. Chem. Solids **61**, 461 (2000).

[34] O. Hellman, P. Steneteg, I. A. Abrikosov, and S. I. Simak, Temperature dependent effective potential method for accurate free energy calculations of solids, Phys. Rev. B **87**, 104111 (2013).

[35] O. Hellman and I. A. Abrikosov, Temperature-dependent effective third-order interatomic force constants from first principles, Phys. Rev. B **88**, 144301 (2013).

[36] G. Sun, J. Kürti, P. Rajczy, M. Kertesz, J. Hafner, and G. Kresse, Performance of the Vienna *ab initio* simulation package (VASP) in chemical applications, J. Mol. Struct. **624**, 37 (2003).

[37] J. P. Perdew, K. Burke, and Y. Wang, Generalized gradient approximation for the exchange-correlation hole of a many-electron system, Phys. Rev. B **54**, 16533 (1996).

[38] Y. Li, J. Liu, and J. Hong, Anharmonicity-induced strong temperature-dependent thermal conductivity in $CuInX_2$ (X= Se, Te), Phys. Rev. B **106**, 094317 (2022).

[39] J. H. Lloyd-Williams and B. Monserrat, Lattice dynamics and electron-phonon coupling calculations using nondiagonal supercells, Phys. Rev. B **92**, 184301 (2015).

[40] Z. Han, X. Yang, W. Li, T. Feng, and X. Ruan, FOURPHONON: An extension module to SHENGBTE for computing four-phonon scattering rates and thermal conductivity, Comput. Phys. Commun. **270**, 108179 (2022).

[41] W. Li, J. Carrete, N. A. Katcho, and N. Mingo, SHENGBTE: A solver of the Boltzmann transport equation for phonons, Comput. Phys. Commun. **185**, 1747 (2014).

[42] See Supplemental Material at http://link.aps.org/supplemental/10.1103/PhysRevB.109.174302 for the convergence of the cut-off distance to extract second-, third-, and fourth-order force constants; the convergence test of q mesh for thermal conductivity calculation; the thermal conductivity of different half-Heusler materials at 300 K; the cumulative thermal conductivity and energy-dependent thermal conductivity of LuNiBi at 300 K; the three-phonon scattering phase space and the phonon dispersion of LuNiBi at 700 K; the formula of phonon self-energy calculation; diagrams representing contributions to the phonon shift Δ and phonon linewidth Γ; a table of the thermal conductivity of different half-Heusler materials.

[43] N. Shulumba, O. Hellman, and A. J. Minnich, Intrinsic localized mode and low thermal conductivity of PbSe, Phys. Rev. B **95**, 014302 (2017).

[44] R. S. Tripathi and K. N. Pathak, Self-energy of phonons in an anharmonic crystal to $O(\Delta 4)$, Nuovo Cimento B **21**, 289 (1974).

[45] P. Procacci, G. Cardini, R. Righini, and S. Califano, Anharmonic lattice dynamics and computer simulation for simple model systems, Phys. Rev. B **45**, 2113 (1992).

[46] M. Balkanski, R. F. Wallis, and E. Haro, Anharmonic effects in light scattering due to optical phonons in silicon, Phys. Rev. B **28**, 1928 (1983).

[47] K. Momma and F. Izumi, VESTA: A three-dimensional visualization system for electronic and structural analysis, J. Appl. Crystallogr. **41**, 653 (2008).

[48] L. Allan, W. M. Mulwa, J. M. Mwabora, R. J. Musembi, and R. E. Mapasha, An *ab-initio* study of P-type ZrCoY (Y = Sb and Bi) half-Heusler semiconductors, Heliyon **9**, e18531 (2023).

[49] L. Xie, J. H. Feng, R. Li, and J. Q. He, First-principles study of anharmonic lattice dynamics in low thermal conductivity $AgCrSe_2$: Evidence for a large resonant four-phonon scattering, Phys. Rev. Lett. **125**, 245901 (2020).

[50] Y. Wang, Q. Gan, M. Hu, J. Li, L. Xie, and J. He, Anharmonic lattice dynamics and the origin of intrinsic ultralow thermal conductivity in AgI materials, Phys. Rev. B **107**, 064308 (2023).

[51] H. Zhu *et al.*, Discovery of ZrCoBi Based half Heuslers with high thermoelectric conversion efficiency, Nat. Commun. **9**, 2497 (2018).

[52] T. Sekimoto, K. Kurosaki, H. Muta, and S. Yamanaka, Thermoelectric and thermophysical properties of TiCoSb-ZrCoSb-HfCoSb pseudo ternary system prepared by spark plasma sintering, Mater. Trans. **47**, 1445 (2006).

[53] S. Li *et al.*, *n*-type TaCoSn-based half-Heuslers as promising thermoelectric materials, ACS Appl. Mater. Interfaces **11**, 41321 (2019).

[54] J. Mao, J. Zhou, H. Zhu, Z. Liu, H. Zhang, R. He, G. Chen, and Z. Ren, Thermoelectric properties of *n*-type ZrNiPb-based half-Heuslers, Chem. Mater. **29**, 867 (2017).

[55] H. Zhu *et al.*, Discovery of TaFeSb-based half-Heuslers with high thermoelectric performance, Nat. Commun. **10**, 270 (2019).

[56] S. Mukhopadhyay, L. Lindsay, and D. S. Parker, Optic phonon bandwidth and lattice thermal conductivity: The case of Li_2X (X= O, S, Se, Te), Phys. Rev. B **93**, 224301 (2016).

[57] L. F. Huang, P. L. Gong, and Z. Zeng, Correlation between structure, phonon spectra, thermal expansion, and thermomechanics of single-layer MoS_2, Phys. Rev. B **90**, 045409 (2014).

[58] P.-F. Liu, T. Bo, J. Xu, W. Yin, J. Zhang, F. Wang, O. Eriksson, and B.-T. Wang, First-principles calculations of the ultralow thermal conductivity in two-dimensional group-IV selenides, Phys. Rev. B **98**, 235426 (2018).

[59] P.-F. Liu, T. Bo, Z. Liu, O. Eriksson, F. Wang, J. Zhao, and B.-T. Wang, Hexagonal M_2C_3 (M= As, Sb, and Bi) monolayers: New functional materials with desirable band gaps and ultrahigh carrier mobility, J. Mater. Chem. C **6**, 12689 (2018).

[60] L. F. Huang and Z. Zeng, Lattice dynamics and disorder-induced contraction in functionalized graphene, J. Appl. Phys. **113**, 083524 (2013).

[61] N. K. Ravichandran and D. Broido, Phonon-phonon interactions in strongly bonded solids: Selection rules and higher-order processes, Phys. Rev. X **10**, 021063 (2020).

[62] J. M. Ziman, *Electrons and Phonons* (Oxford University, New York, 1960).